RSC Advances

PAPER

View Article Online
View Journal | View Issue

Cite this: *RSC Adv.*, 2025, **15**, 41862

Magnetic AuNPs@TiO_2@NF heterojunction for solar-light degradation of antibiotics and mitigation of bacterial resistance risk

Joanna Breczko, [a] Anna Basa, [a] Katarzyna Niemirowicz-Laskowska, [b] Beata Skonieczna, [b] Raúl López-Martín, [cd] Jose A. De Toro, [cd] Halina Car [b] and Elzbieta Regulska *[ace]

Antibiotic resistance is a silent crisis unfolding in slow motion, and sustainable solutions are urgently needed. We developed a solar-powered, magnetically recoverable Au@TiO_2@NF photocatalyst that degrades 91% of tigecycline in 33 minutes and eliminates its toxicity. The material's porous SiO_2-templated framework (53 m^2 g^{-1}) integrates plasmonic gold nanoparticles and magnetic nickel ferrite (NF), optimizing light absorption and recyclability. Structural analysis confirmed crystalline anatase TiO_2 and cubic NF phases, while electron microscopy revealed an interconnected porous network that enhances reactivity. Radical scavenger experiments identified superoxide radicals ($^{\bullet}O_2^-$) are the primary active species, with photogenerated holes and hydroxyl radicals ($^{\bullet}OH$) playing complementary roles. This synergistic action is enhanced by our material's design: plasmonic gold injects hot electrons, while the tailored interface between TiO_2 and NF promotes efficient charge separation, yielding a 3.6-fold efficiency gain over TiO_2 alone. The catalyst is stable across a broad pH range (4.5–10) and is fully recovered post-reaction using a magnet, preventing secondary nanoparticle pollution. Degradation byproducts show no cytotoxicity in human fibroblasts, monocytes, or hepatocytes and reduce pro-inflammatory TNF-α by 40–60%. Crucially, it preserves CYP3A4 activity, avoiding drug-interaction risks. The material also functions as an electrochemical H_2O_2 sensor (LOD: 0.0447 mM), demonstrating multifunctionality. This work shows promise for antibiotic wastewater treatment. The solar-driven approach is efficient and environmentally safe.

Received 3rd September 2025
Accepted 23rd October 2025

DOI: 10.1039/d5ra06637a

rsc.li/rsc-advances

Introduction

Water pollution poses one of the most pressing challenges to the environment and human health.[1,2] Conventional remediation technologies struggle to address persistent contaminants, including organic pollutants and heavy metals.[3–6] Photocatalysis has emerged as a promising solution for water remediation due to its ability to harness light energy for pollutant degradation.[7,8] However, its widespread application is hindered by several limitations: (i) narrow spectral response (<5% solar spectrum utilization), (ii) inefficient charge separation (>80% recombination losses), and (iii) impractical catalyst recovery.[9,10] Our work overcomes these challenges through an innovative materials design that integrates plasmonics, semiconductor engineering, and magnetic nanotechnology.

Antibiotics such as TG persist in wastewater due to their resistance to conventional treatment, promoting the development of antibiotic-resistant bacteria (ARB) – a critical public threat. The World Health Organization (WHO) ranks antibiotic resistance among the top global health risks, projecting 10 million annual deaths by 2050 if left unaddressed. Photocatalytic degradation offers a viable strategy to mineralize antibiotics before they enter ecosystems, thereby reducing selective pressure for resistance genes. However, the intermediates generated during incomplete degradation (*e.g.*, hydroxylated or demethylated derivatives) must also be evaluated, as some may retain biological activity or introduce new toxicological risks.

An effective photocatalyst must fulfill two critical criteria: (1) visible-light activity to harness abundant solar energy, and (2) generation of long-lived electron–hole pairs and reactive oxygen species (ROS) to ensure sustained photocatalytic efficiency. Metal nanoparticles (NPs), particularly plasmonic AuNPs, offer a compelling solution to the limited visible-light absorption of conventional photocatalysts.[11] Their localized surface plasmon

[a]*Faculty of Chemistry, University of Bialystok, Ciolkowskiego 1K, 15-245 Bialystok, Poland*

[b]*Department of Experimental Pharmacology, Medical University of Bialystok, Szpitalna 37, 15-295 Bialystok, Poland*

[c]*Instituto Regional de Investigación Científica Aplicada (IRICA), University of Castilla-La Mancha, Avenida Camilo José Cela 1, 13071, Ciudad Real, Spain*

[d]*Departamento de Física Aplicada, Universidad de Castilla-La Mancha, 13071 Ciudad Real, Spain*

[e]*Faculty of Pharmacy, University of Castilla-La Mancha, Almansa 14, 02008 Albacete, Spain. E-mail: elzbieta.regulska@uclm.es*

resonance (LSPR) effect enables strong light absorption across the visible spectrum, while also acting as electron sinks to reduce charge recombination. When integrated into composite systems, AuNPs can generate hot electrons under illumination, injecting them into semiconductor materials like TiO_2 to initiate redox reactions.[12] This synergistic effect not only broadens the photocatalytic activity window but also enhances degradation efficiency for stubborn pollutants. Titanium dioxide (TiO_2) remains one of the most widely studied photocatalysts due to its chemical stability, non-toxicity, and robust redox potential. Coating AuNPs with TiO_2 creates a Schottky junction at the metal–semiconductor interface, further suppressing electron–hole recombination.[13] The anatase phase of TiO_2, in particular, offers optimal photocatalytic activity, while its mesoporous forms increase surface area for pollutant adsorption. By combining TiO_2 with plasmonic AuNPs, we leverage both the UV activity of TiO_2 and the visible-light response of AuNPs, creating a broadband photocatalytic system.

Magnetic components like nickel ferrite ($NiFe_2O_4$) address the critical challenge of catalyst recovery. Their inherent ferromagnetism allows for facile separation using external magnetic fields, eliminating the need for energy-intensive filtration or centrifugation.[14] Beyond separation, $NiFe_2O_4$ itself exhibits photocatalytic properties under visible light due to its narrow bandgap,[15,16] complementing the TiO_2@AuNP system.[17] Additionally, magnetic materials can enhance charge separation by acting as electron reservoirs, further boosting catalytic efficiency.[18]

In this study, we engineer a magnetic powerhouse for photo- and electrocatalysis: a gold-embedded TiO_2@$NiFe_2O_4$ ternary composite designed for efficient antibiotic degradation. By architecting a void-rich framework *via* SiO_2 templating, we strategically embed plasmonic AuNPs to maximize surface area and visible-light absorption. Subsequent TiO_2 encapsulation and magnetic $NiFe_2O_4$ deposition yield a multifunctional system where each component plays a synergistic role—AuNPs drive visible-light activity, TiO_2 ensures robust charge generation, and $NiFe_2O_4$ enables magnetic recovery while contributing to catalytic cycles. This unique core–shell design not only overcomes the spectral limitations of conventional photocatalysts but also unifies photocatalytic and electrocatalytic functionalities in a single platform. Our optimized composite addresses three critical challenges simultaneously: (1) solar energy utilization, (2) electron–hole pair longevity, and (3) practical catalyst reusability, marking a transformative step toward sustainable water remediation.

Results and discussion

X-ray diffraction analysis confirmed the crystalline structure of TiO_2 and $NiFe_2O_4$ as components of the AuNPs@TiO_2@NF composite (see Fig. 1a). The gold-embedded TiO_2 (AuNPs@TiO_2) consists of anatase-phase titanium dioxide surrounding the gold core. The characteristic diffraction peaks of TiO_2 are observed at 25.1°, 36.3°, 37.1°, 47.7°, 53.6°, 54.8°,

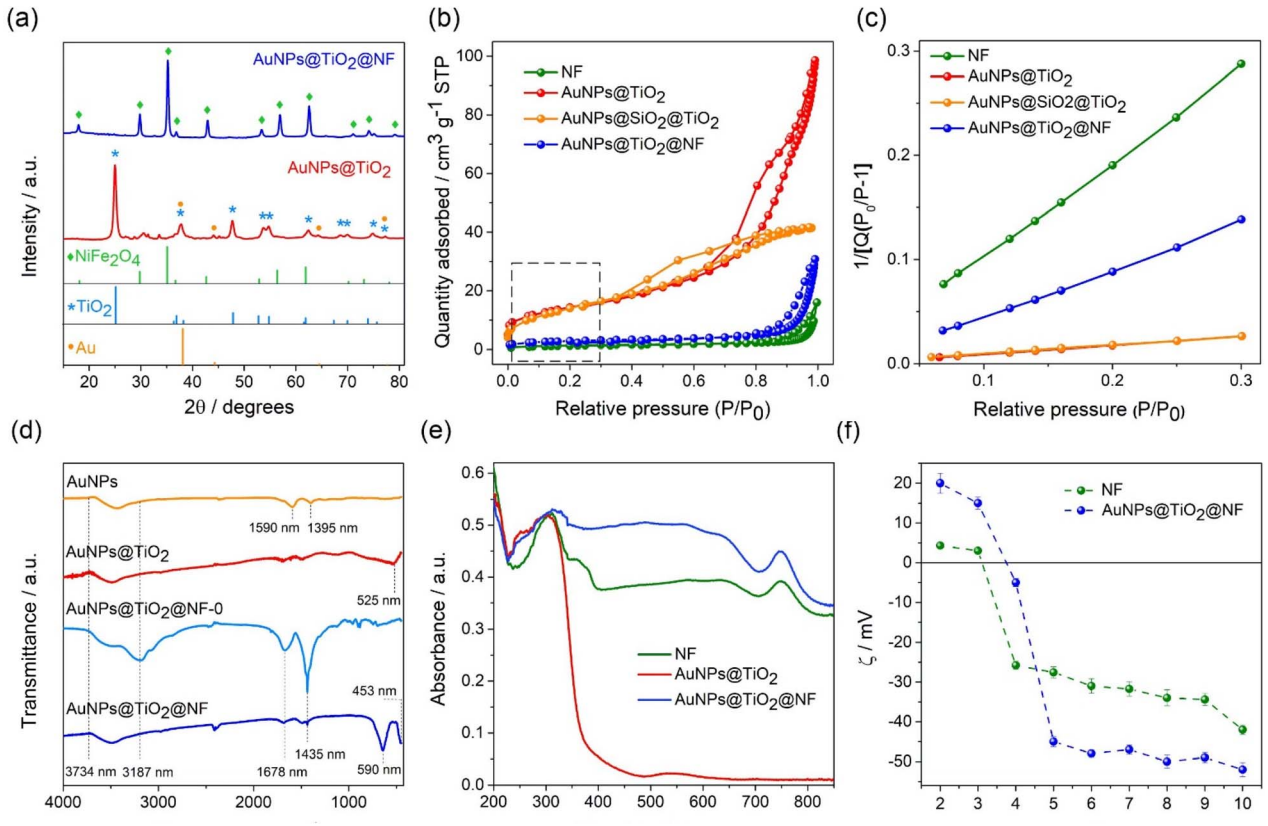

Fig. 1 (a) PXRD patterns, (b) N_2 adsorption–desorption isotherms, (c) BET plots for the region marked in (b), (d) IR, (e) UV-Vis, and (f) ELS data.

62.3°, 68.5°, 70.1°, 74.8°, and 77.1°, corresponding to the planes (101), (103), (004), (200), (105), (211), (204), (116), (220), (215), and (301) of anatase.[19] Additional peaks at 37.6°, 44.1°, 64.3°, and 77.4° are attributed to the gold core within the AuNPs@TiO_2.[20] In the AuNPs@TiO_2@NF composite, the diffraction pattern is dominated by peaks associated with $NiFe_2O_4$, with signals at 18.0°, 29.8°, 35.1°, 37.0°, 42.8°, 53.5°, 56.9°, 62.4°, 70.9°, 74.0°, and 79.1°, corresponding to the planes (111), (220), (311), (222), (400), (422), (511), (440), (620), (533), (444), and (642) of cubic nickel ferrite.[21]

Transmission electron microscopy (TEM) revealed the size of the pristine gold nanoparticles (AuNPs) to be within the range of 15–30 nm (Fig. 2a and b). The selected-area electron diffraction (SAED) highlighted the (111) plane of AuNPs (Fig. 2c and d). The modification of the AuNPs with the titanium dioxide increased the gold core up to a diameter of 85–100 nm (Fig. 2e and f). SAED measurements confirmed the presence of TiO_2 around the AuNPs core, as indicated by (101) planes (Fig. 2g). The final AuNPs@TiO_2@NF composite was covered by nickel ferrite (Fig. 2i). The energy-dispersive X-ray (EDX) spectroscopy depicted all elements present in AuNPs@TiO_2@NF, *i.e.* Au, Ti, O, Ni, and Fe (Fig. 2j and k).

The morphology of the materials obtained throughout the synthesis of the AuNPs@TiO_2@NF composite was further investigated by scanning electron microscopy (SEM) (Fig. 3). AuNPs covered only with silicon dioxide matrix occurred as rectangular flakes (Fig. 3a and e). The AuNPs embedded in titanium dioxide, AuNPs@TiO_2, were prepared through covering with titanium dioxide and subsequent removal of silicon dioxide matrix. The thereby obtained AuNPs@TiO_2 composite had a regular porous structure (Fig. 3b and f). Further modification of AuNPs@TiO_2 with nickel ferrite enriched the final AuNPs@TiO_2@NF composite with a more complex morphology. Fig. 3c, d, g and h demonstrates a cheese-like structure (Fig. 3d) with additional tube-shaped channels in AuNPs@TiO_2@NF (Fig. 3g and h).

The porosity was further examined with liquid nitrogen adsorption–desorption measurements recorded for NF, AuNPs@TiO_2, AuNPs@SiO_2@TiO_2 and AuNPs@TiO_2@NF are shown in Fig. 1b and c. The characteristic hysteresis loop and *t*-

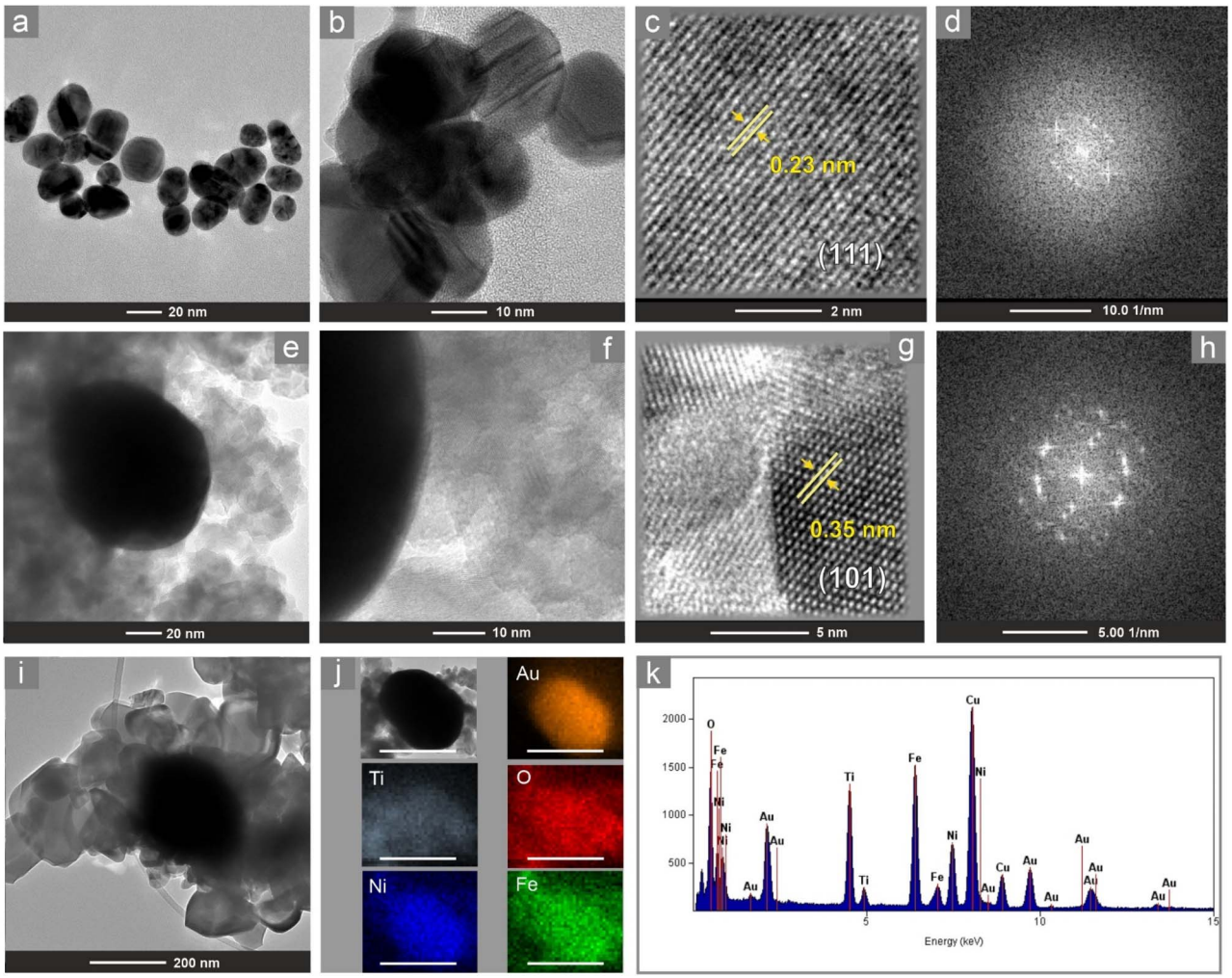

Fig. 2 (a–c, e–g and i) TEM images, (d and h) SAED patterns, (j) EDX images, and (k) EDX profile of (a–d) AuNPs, (e–h) AuNPs@TiO_2, and (i–k) AuNPs@TiO_2@NF. Scale bar of 500 nm in (j).

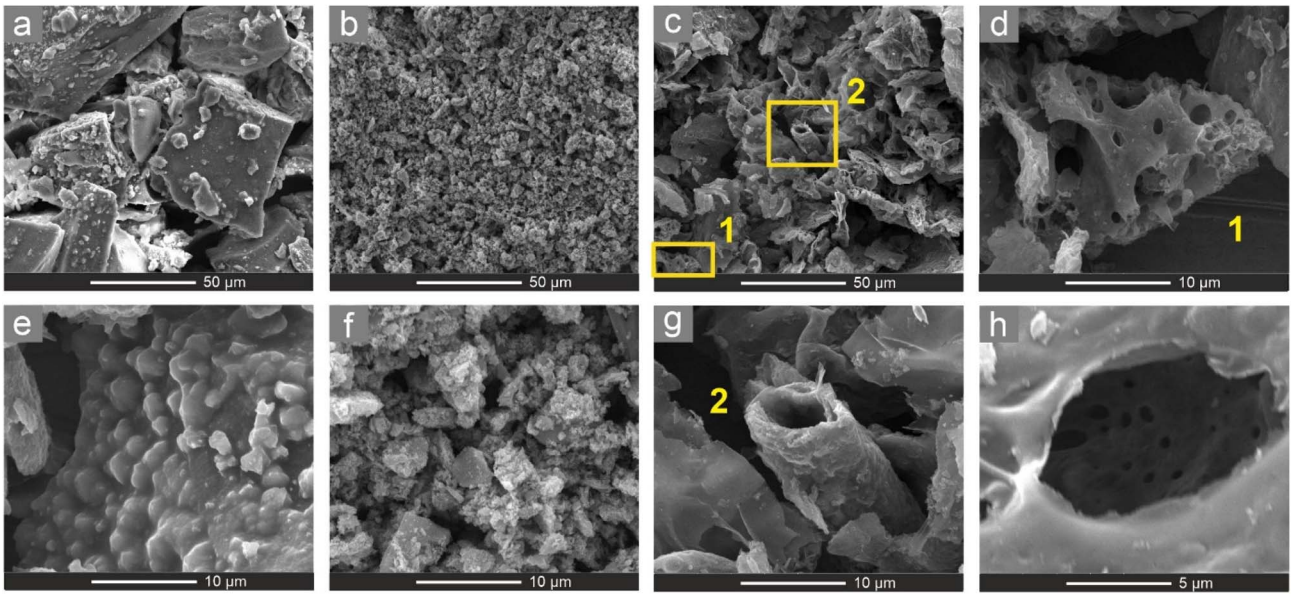

Fig. 3 SEM images of (a and e) AuNPs@SiO_2, (b and f) AuNPs@TiO_2, (c d, g and h) AuNPs@TiO_2@NF.

plot analysis of the recorded isotherms confirmed the dominance of mesopores in the synthesized materials.[22] Textural parameters such as specific surface area, cumulative volume of pores and average pore diameter, obtained using Brunauer–Emmett–Teller (BET) and Barrett–Joyner–Halenda (BJH) calculations, are summarized in Table 1.

The BET surface area (SBET) of pristine NF was found to be 5 $m^2\ g^{-1}$, which is consistent with values reported in the literature for $NiFe_2O_4$, where SBET can be as low as 3 $m^2\ g^{-1}$.[23,24] Incorporating gold and titanium oxide NPs, known for their high mesoporosity,[25] into the spinel structure enhanced the SBET to 10 $m^2\ g^{-1}$ and the total pore volume to 0.0458 $cm^3\ g^{-1}$ in the AuNPs@TiO_2@NF composite, reaching nearly double the values of the pristine NF (Fig. 1b, Table 1). However, these values remain lower than those observed for the reference AuNPs@TiO_2 and AuNPs@SiO_2@TiO_2 (Table 1), indicating partial agglomeration of the composite.[26] This is further evidenced by the increased nanoparticle size and the expansion of the inter-crystallite/aggregate distance in the AuNPs@TiO_2@NF material (Table 1). The mean pore diameter, determined by the BJH method, was 31.7 nm for AuNPs@TiO_2@NF, which falls within the mesoporous range (2–50 nm).[27] The observed increase in pore size compared to pristine spinel (d_{pore} = 28.1 nm) indicates the enhanced surface area of the new AuNPs@TiO_2@NF system (Table 1).

Table 1 Parameters determined from nitrogen adsorption–desorption measurements for the synthesized materials

Material	BET surface area/$m^2\ g^{-1}$	Cumulative volume of pores[a]/$cm^3\ g^{-1}$	Average pore diameter[b]/nm
NF	5	0.0241	28
AuNPs@TiO_2	51	0.1511	12
AuNPs@TiO_2@NF	10	0.0458	32
AuNPs@SiO_2@TiO_2	53	0.0837	6

[a] BJH adsorption cumulative volume of pores between 17 000–3 000 000 Å diameter. [b] BJH adsorption average pore diameter (4*V*/*A*).

We performed the infrared spectroscopy measurements to investigate the surface groups of the composites (Fig. 1d). First of all, we confirmed the chemical composition of the bi- and ternary composites. The AuNPs@TiO_2 material has a characteristic band at 525 cm^{-1} arising from the Ti–O stretching vibrations.[28] The broader band spanning from 3187 nm to 3734 nm derives from the surface hydroxylic groups. Further functionalization of the binary composite with the nickel ferrite enriched the ternary composite with the intense band at 1435 cm^{-1}, and a broad band with the maximum at 3187 cm^{-1}, an indication of O–H bending and stretching vibrations, respectively, from the carboxylic acid. The band with a maximum at 1435 cm^{-1} also contributed to the symmetric vibrations of the nitrate ions.[29] The band at 1678 cm^{-1} arose from the C=O stretching modes of the citric acid and asymmetric stretching vibrations of the nitrate. Upon calcination of the AuNPs@TiO_2@NF-0, the precursors of the $NiFe_2O_4$ were decomposed, and amorphous nickel ferrite was transformed to its crystalline form. It is demonstrated by the disappearance of the above-listed bands and a rise of bands at 590 cm^{-1} and 430 cm^{-1} deriving from stretching vibrations of Fe–O in tetrahedral sites and metal–O in octahedral sites, respectively.[30] Importantly, the calcinated AuNPs@TiO_2@NF contained surface hydroxyl groups as demonstrated by the broad bands within 3187–3734 cm^{-1}.

UV-Vis spectroscopy demonstrated that the AuNPs@TiO_2@NF composite effectively absorbs light across the contrasts sharply with the AuNPs@TiO_2 composite, which primarily absorbs in the UV region due to the TiO_2 component

and exhibits a low-intensity broad band, peaking around 530 nm, attributed to the AuNPs.[31] In comparison, the AuNPs@TiO_2@NF composite displays a distinct absorption with a maximum at 750 nm, confirming the presence of nickel ferrite.

Electrophoretic light scattering analysis revealed that the AuNPs@TiO_2@NF composite exhibits stability across a broad pH range of 4.5–10, with zeta (ζ) potential values consistently exceeding −30 mV and reaching up to 50 mV in most of this range (Fig. 1f). This represents a notable enhancement compared to pristine nickel ferrite (NF), which shows a ζ potential of approximately −35 mV within the same pH interval. The surface charge of the AuNPs@TiO_2@NF composite is positive at pH values below 3.7 and negative at pH values above 3.7. This may appear unfavorable for TG adsorption across the entire pH range, as TG contains multiple ionizable groups with distinct pK_a values (2.8, 4.4, 7.4, 8.9, 9.5).[32] At pH < 3, TG carries a positive charge due to protonation of its hydroxyl and amino groups. In the pH range between 3 and 9.5, TG predominantly exists in a zwitterionic form, while at pH > 9.5, the deprotonation of amino groups (pK_a 8.9 and 9.5) results in a negatively charged antibiotic. However, since the photocatalytic degradation experiments were conducted at neutral pH, no incompatibility was observed between TG adsorption and the AuNPs@TiO_2@NF composite surface.

We observed that NF (Fig. 4a and b) and both NF-based composites (NF@TiO_2@Au: Fig. 4c and d; Au@TiO_2@NF: Fig. 4e and f) show attraction to the neodymium magnet. This behavior is beneficial for a photocatalyst, since it would ease the separation of the photocatalyst from the remediated medium and might substantially lower the purification costs while applied on a larger scale. The room temperature (300 K) hysteresis loops of the different samples can be found in Fig. 4, where the magnetic moment is normalized in two different ways: to the total mass (Fig. 4g) and to the mass of nickel ferrite (Fig. 4h). From either one, it is clear that all composites show soft magnetic behavior as expected from their ferrimagnetic nickel ferrite content. Specifically, Au@TiO_2@NF shows higher saturation magnetization, M_S, than the other two composites, due to its higher NF content (see Fig. 4g). Indeed, the 54 wt% NF content in Au@TiO_2@NF compared to the approximately 3.6 wt% in the other two cases (see Table 2) makes Au@TiO_2@NF the best candidate for magnetic recovery.

On the other hand, Fig. 4h shows a modification of the magnetic behavior of the nickel ferrite in the composites. Note that this figure shows the magnetization of the sample per unit mass of NF. Therefore, this figure effectively describes the magnetic behavior of the NF in the samples, for it is the only magnetic component in the composites. The magnetization of the ferrite in the composites decreases around one-third with

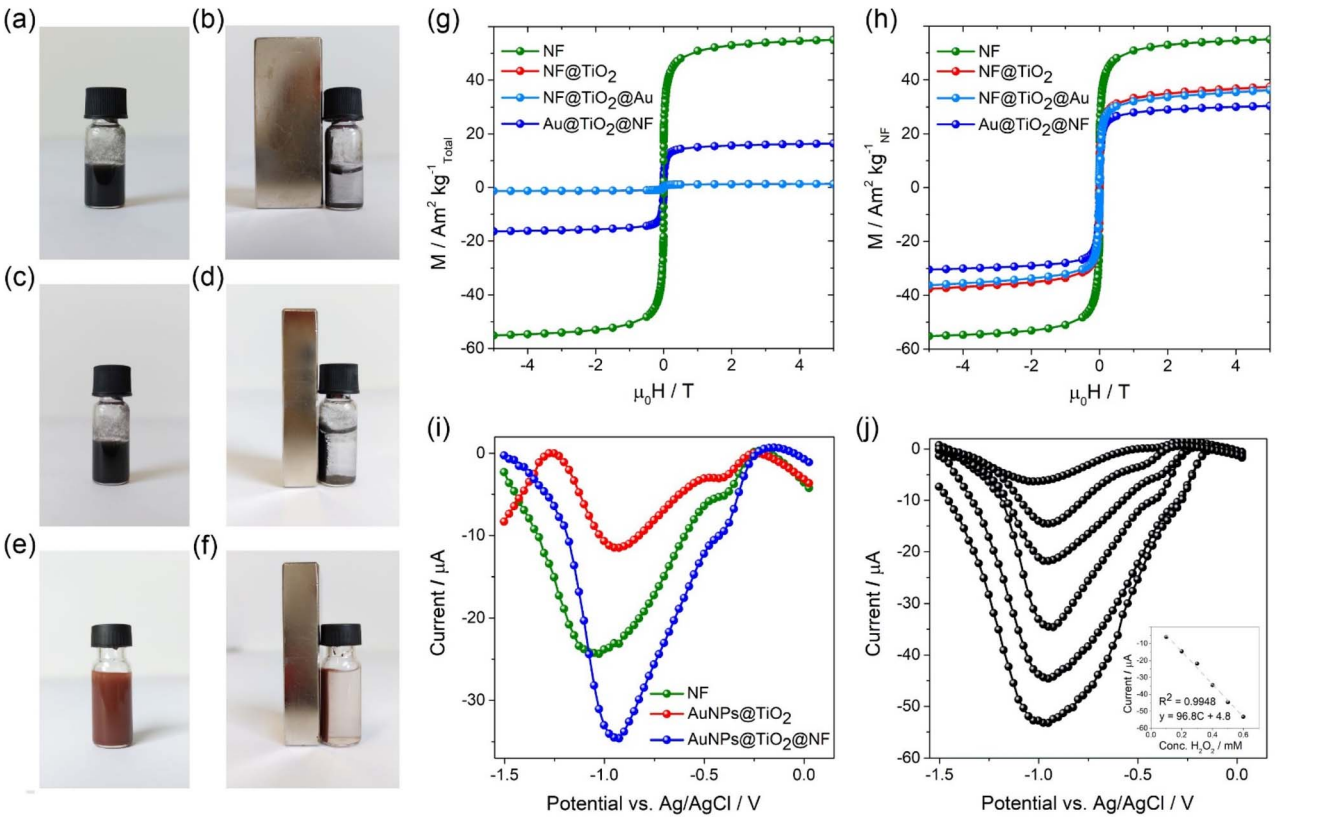

Fig. 4 Images of (a and b) NF, (c and d) NF@TiO_2, and (e and f) Au@TiO_2@NF in water. Magnetic hysteresis loops at 300 K normalized (g) to the total mass of the composite and (h) to the mass of nickel ferrite. (i) DPV curves of electrocatalytic reduction of H_2O_2 in 0.01 mol per L PBS using GCE electrode modified with different materials. (j) DPV curves for different concentrations of hydrogen peroxide determined on Au/TiO_2/NF/GCE in 0.01 M PBS. Inset: calibration curve.

Table 2 Magnetic properties of the samples obtained from the room temperature loops

Sample	M_S (A m^2 kg$_{TOTAL}^{-1}$)	M_S (A m^2 kg$_{NF}^{-1}$)	$\mu_0 H_C$ (mT)	M_R/M_S
NF	55.1	55.1	0.2	0.004
NF@TiO_2	1.33	37.3	5.16	0.229
NF@TiO_2@AuNPs	1.29	36.2	13.34	0.200
AuNPs@TiO_2@NF	14.8	27.3	5.42	0.162

respect to the pure NF sample, which shows a similar value (55 A m^2 kg^{-1}) to bulk nickel ferrite.[33,34] This points to the formation of complexes between the NF and the titanium dioxide that reduce the overall moment. Interestingly, the NF magnetization in the Au@TiO_2@NF composite is further decreased. Coercivity and remanence values (listed in Table 2 together with the M_S values) also differ from the bulk (NF) values, which may be ascribed to the above-mentioned formation of complexes or simply to the creation of single-domain regions as a result of their mixture with TiO_2. In any scenario, the low coercivity and remanence of AuNPs@TiO_2@NF compared with the other composites, in particular with NF@TiO_2@AuNPs (which exhibits a coercivity as high as 13.3 mT), also makes this sample the best candidate for magnetic separation (now in terms of colloidal stability). In summary, the AuNPs@TiO_2@NF sample shows the highest saturation magnetization and the softest properties of all the samples under study.

The electrocatalytic behavior of AuNPs@TiO_2, NF, and AuNPs@TiO_2@NF composites was evaluated as electrode modifiers for hydrogen peroxide (H_2O_2) detection. Using differential pulse voltammetry (DPV) in 0.01 mol per L PBS (pH = 7.4), the modified electrodes exhibited a dramatically enhanced current during H_2O_2 electroreduction compared to unmodified surfaces (see Fig. 4i). The reduction peak potentials were observed at −0.93 V (AuNPs@TiO_2), −1.08 V (NF), and −0.95 V (AuNPs@TiO_2@NF), with the AuNPs@TiO_2@NF/GCE system demonstrating the highest sensitivity toward H_2O_2. This highlights the superior synergistic effect between the Au–TiO_2 interface and the NF support, optimizing electron transfer kinetics.

Further DPV analysis (Fig. 4j) revealed a linear current-concentration relationship (I (μA) = −96.8C + 4.8, R^2 = 0.9948), confirming robust electrocatalytic activity across a wide H_2O_2 range. The composite achieved a low detection limit (0.0447 mmol L^{-1}, S/N = 3) and an exceptional sensitivity of 48.17 μA L mol^{-1} cm^{-2}, derived from the calibration slope and electrode geometry.[35,36] These findings underscore the strong electrocatalytic potential of AuNPs@TiO_2@NF for advanced (bio)sensing applications, where rapid and precise H_2O_2 quantification is critical.

The AuNPs@TiO_2@NF composite exhibited exceptional photocatalytic activity for the degradation of tigecycline (TG) under simulated solar light, achieving 91% degradation efficiency within 2 hours (Fig. 5a–c and Table 3). In contrast, pristine NF (32%) and AuNPs@TiO_2 (50%) showed significantly lower performance, underscoring the synergistic effects of the ternary composite. The degradation followed pseudo-first-order kinetics, as evidenced by the linear relationship in the logarithmic plots of C_t/C_0 *versus* time (Fig. S1). The half-life of TG with AuNPs@TiO_2@NF was six times shorter than with NF and four times shorter than with AuNPs@TiO_2, demonstrating the composite's superior catalytic efficiency.

Furthermore, we demonstrated that the spatial arrangement of the composite components strongly influenced photocatalytic performance. The AuNPs@TiO_2@NF configuration, where gold nanoparticles (AuNPs) are embedded within TiO_2 and coated with NF, outperformed the NF@TiO_2@AuNPs variant (with surface-deposited AuNPs) by 21% in degradation efficiency and reduced the half-life by 200%. We propose that this enhancement arises from a cascade of charge-transfer processes. Under solar irradiation, the nickel ferrite outer layer absorbs photons and generates excited electrons, which are subsequently injected into the titania conduction band. These photogenerated electrons are then effectively captured and stabilized by the encapsulated gold nanoparticles, creating a unidirectional electron flow that minimizes charge recombination and maximizes photocatalytic activity.

To further elucidate the degradation mechanism, we conducted detailed scavenger experiments using the optimal AuNPs@TiO_2@NF catalyst in the tetracycline degradation process. The introduction of specific radical scavengers provided critical insights into the active species involved (Fig. 5c). The most pronounced suppression was observed after the addition of benzoquinone (BQ, a $^{\bullet}O_2^-$ scavenger), with the degradation efficiency dropping drastically from 91% to 46%. This identifies superoxide radicals as the primary reactive oxygen species. A significant decrease to 53% occurred with ammonium oxalate (AO, a hole scavenger), indicating that holes also play a crucial role, likely by generating oxidative species or directly oxidizing pollutants. The addition of isopropanol (i-PrOH, a $^{\bullet}OH$ scavenger) and dimethyl sulfoxide (DMSO, also a $^{\bullet}OH$ scavenger) reduced the efficiency to 75% and 64%, respectively, confirming the involvement of hydroxyl radicals. These results clearly demonstrate that the photocatalytic process involves multiple active species, with superoxide radicals being the most dominant, followed by holes and hydroxyl radicals.

Our comprehensive electrochemical characterization provides further compelling evidence for the enhanced performance of the Au@TiO_2@NF composite. Through electrochemical impedance spectroscopy (EIS) measurements of NF, Au@TiO_2, and Au@TiO_2@NF-modified glassy carbon electrodes (GCEs), we gained critical insights into the electronic properties governing their photocatalytic behavior. By applying the fundamental Mott–Schottky eqn (1),

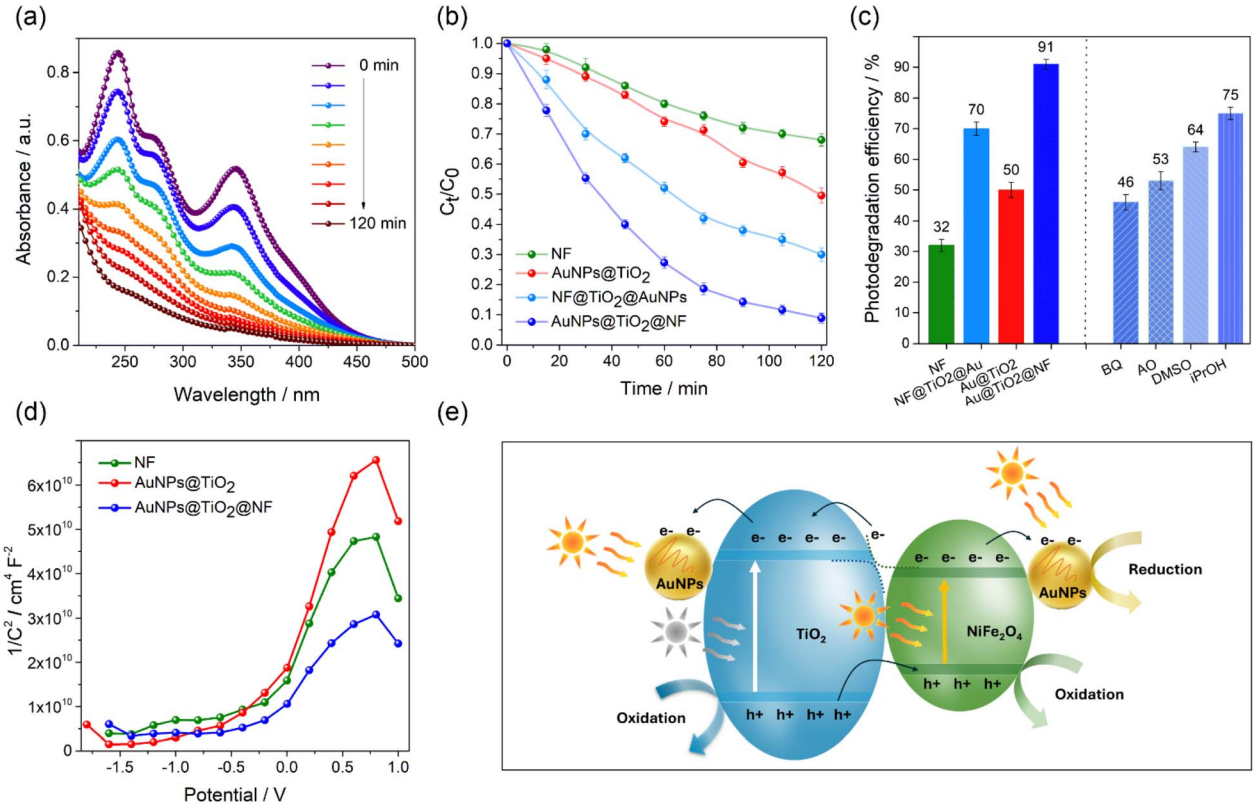

Fig. 5 (a) UV-Vis absorption of TG in the presence of AuNPs@TiO_2@NF. (b) C_t/C_0 *vs.* time and (c) photodegradation efficiency for TG with NF, NF@TiO_2@AuNPs, AuNPs@TiO_2, and AuNPs@TiO_2@NF. (d) Mott–Schottky plots for NF, AuNPs@TiO_2, and AuNPs@TiO_2@NF. (e) Proposed photocatalytic mechanism of AuNPs@TiO_2@NF.

Table 3 Parameters determined for the photocatalytic studies

Material	Photocatalytic degradation efficiency/%	t/min	k/min^{-1}
NF	32	204	0.0034
NF@TiO_2@AuNPs	70	67	0.0104
AuNPs@TiO_2	50	131	0.0053
AuNPs@TiO_2@NF	91	33	0.0209

Table 4 Flat band potentials derived from Mott–Schottky analysis

Material	E_{fb} (V)
NF	−0.39
AuNPs@TiO_2	−0.35
AuNPs@TiO_2@NF	−0.42

$$\frac{1}{C^2} = \frac{2}{\varepsilon\varepsilon_0 e N_A}\left(E_{fb} - E - \frac{kT}{e}\right) \quad (1)$$

where: ε is the dielectric constant of the semiconductor, ε_0 is the dielectric constant of vacuum, e is the electron charge, N_A is the charge carrier density, kT represents the thermal energy, and E is the applied potential, we precisely determined the flat band potentials (E_{fb}) (see Fig. 5d), which represent the potential at which the semiconductor-electrolyte interface remains unpolarized and electrically neutral.[37] The calculated E_{fb} values determined for NF, AuNPs@TiO_2, and Au@TiO_2@NF (Table 4) inform on the potential at which the semiconductor|electrolyte interfacial region remains unpolarized, meaning when the semiconductor surface is electrically neutral.[38]

The calculated E_{fb} values demonstrate a progressive cathodic shift from −0.39 V for bare NF to −0.42 V for the ternary AuNPs@TiO_2@NF composite, with the binary AuNPs@TiO_2 system exhibiting an intermediate value of −0.35 V. This negative shift in E_{fb} for the ternary composite signifies several crucial advantages: (1) an elevated fermi level that enhances the thermodynamic driving force for reduction reactions, (2) improved charge separation efficiency through synergistic interactions between components, and (3) stronger overall reduction capability. The intermediate behavior of AuNPs@TiO_2 (−0.35 V) compared to bare NF (−0.39 V) confirms the electron-trapping role of Au nanoparticles.

These electrochemical findings are corroborated by our scavenger experiments, which identified photogenerated electrons as the primary active species. The combined results enable us to propose a coherent reaction mechanism (Fig. 5e). The photocatalytic activity begins with light absorption by TiO_2 (UV-active), NF (visible-light-active), and AuNPs (*via* localized surface plasmon resonance, LSPR), generating electron–hole pairs. The charge transfer pathway, driven by the internal electric field at the heterojunction interface, is critical for

efficiency. Photogenerated electrons are driven from the conduction band (CB) of NF to the CB of TiO_2. Simultaneously, photogenerated holes transfer from the valence band (VB) of TiO_2 to the VB of NF. This spatial charge is further enhanced by the Au nanoparticles, which act as electron sinks, directly trapping electrons from both the CB of TiO_2 and from the CB of NF itself. This multi-point electron scavenging drastically reduces recombination losses. The directed charge flow results in the accumulation of electrons on TiO_2 and AuNPs, which facilitates powerful reduction processes (O_2 to $^{\bullet}O_2^-$, H^+ to H_2). Simultaneously, the holes accumulated on the NF surface are available for oxidation reactions (*e.g.* H_2O to O_2). The system's enhanced reduction power is directly evidenced by the cathodic shift in flat-band potential ($E_{fb} = -0.42$ V). Key advantages of this ternary composite include: (i) broad-spectrum light absorption (UV + visible + plasmonic Au), (ii) exceptional charge separation *via* interface-induced charge transfer and Au electron trapping, and (iii) enhanced electron density for reduction reactions. These synergistic effects make AuNPs@TiO_2@NF a superior photocatalyst for reduction-focused applications like hydrogen production, CO_2 reduction, and pollutant degradation.

The catalyst's stability was confirmed by characterizing the material recovered after five photocatalytic cycles. XRD, SEM, EDX, and FTIR analyses (Fig. S2–S5) show no changes in its crystal structure, morphology, elemental composition, or surface groups, demonstrating robust stability.

The high-performance liquid chromatography coupled with tandem mass spectrometry (LC-MS/MS) analysis provided critical insights into the photocatalytic degradation products of TG using AuNPs@TiO_2@NF. Our results confirmed complete decomposition of TG, with the formation of lower-molecular-weight intermediates and ultimate mineralization into small organic fragments and inorganic species (*e.g.* CO_2, H_2O, NH_3). The superior photocatalytic efficiency of AuNPs@TiO_2@NF over NF@TiO_2@AuNPs (Scheme 1 and Table S1) is evident from the near-total disappearance of TG and the minimal accumulation of detectable intermediates, highlighting its enhanced oxidative capability. The degradation pathway involves initial hydroxylation (*m*/*z* 584.27) and demethylation of TG, introducing polar groups (–OH, –NH_2) that facilitate further breakdown. This is followed by oxidative cleavage (*m*/*z* 491.14, 555.21), advanced dehydroxylation and decarboxylation (*m*/*z* 333.10), and finally mineralization into small carboxylic acids (*m*/*z* 195.05, 159.04) and fragments (*m*/*z* 113.06, 88.99). The scarcity of persistent intermediates with AuNPs@TiO_2@NF—compared to NF@TiO_2@AuNPs—demonstrates its rapid oxidation kinetics, driven by synergistic plasmonic enhancement (AuNPs) and hole-mediated oxidation (TiO_2), as reported in our earlier mechanistic study.[16]

A recent study assessed the cytotoxic effects of oxytetracycline and its photocatalytic degradation products.[39] Following this line of research, the present study investigates the impact of TG and its photocatalytic metabolites on cell viability, metabolic activity, and function across different cell types. The scope of the study was expanded to include additional parameters such as redox balance, immunomodulatory effects, and the activity of xenobiotic-metabolizing enzymes, particularly cytochrome P450 (CYP3A4). Cytotoxicity evaluations were performed under standard culture conditions using human fibroblasts (CCD-1079Sk), monocytic cells (THP-1), and human hepatic cells (HepG2). Cell viability and metabolic activity were assessed *via* MTT assay and neutral red uptake assay.

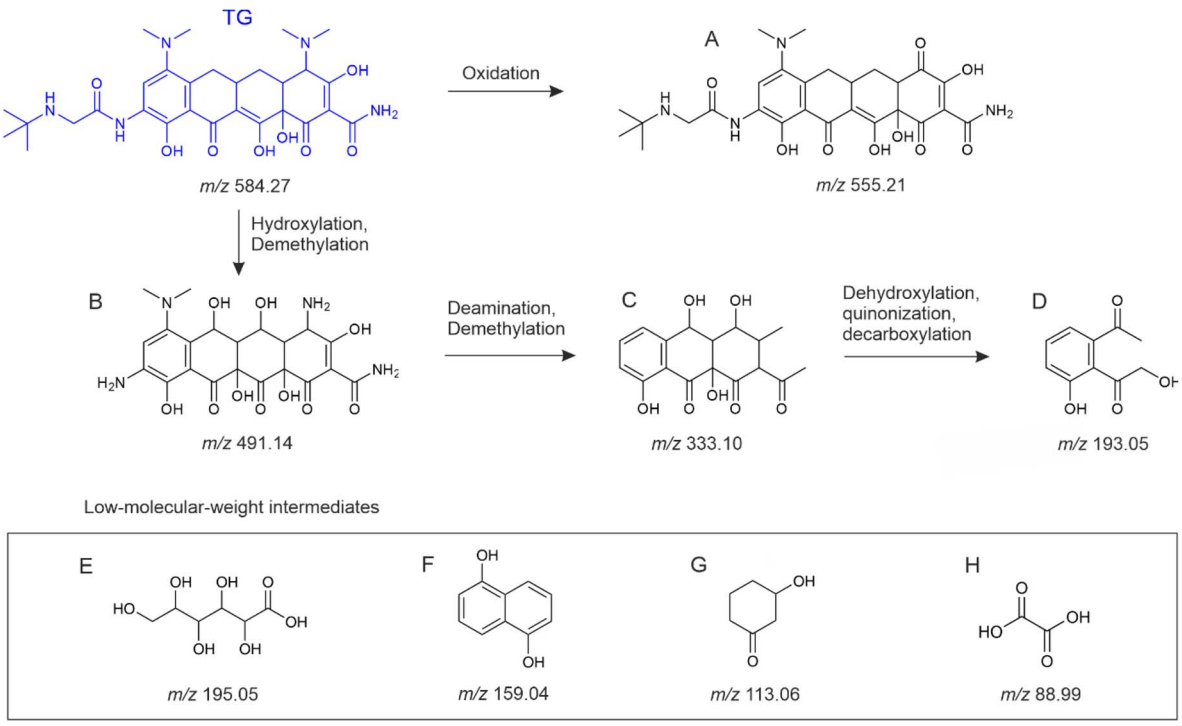

Scheme 1 Proposed photocatalytic degradation pathway of TG in the presence of AuNPs@TiO_2@NF.

Immunomodulatory properties were examined *in vitro* using models both with and without LPS stimulation. Additionally, the influence of TG and its metabolites on CYP3A4 activity was investigated.

In experiments with CCD-1079Sk fibroblasts, cells were exposed to TG and its metabolites at concentrations of 10 μL and 100 μL per well for 24 hours (Fig. 6). Results indicated that at 10 μL, no significant toxicity was observed. However, at the higher concentration (100 μL), varying cytotoxic effects were noted; cell viability remained near 100% with NF, dropped to ~70% with $AuTiO_2$@NF, and fell below 50% with TG and AuNPs@TiO_2 (Fig. 6). Despite these differences, none of the tested agents caused a statistically significant reduction in metabolic activity. To further assess cellular stress responses, NAD^+/NADH ratio and ROS production were measured. The NAD^+/NADH ratio is a critical metabolic regulator, influencing oxidative stress and ATP production. An elevated ratio can enhance cellular defense mechanisms, including DNA repair,[40] while a decreased ratio may disrupt metabolic processes and contribute to pathological conditions.[41] In fibroblasts treated with 10 μL of TG and its metabolites, a significant increase in NAD^+ levels was observed. However, no notable changes in ROS production were detected, suggesting that oxidative stress was not a major factor under these conditions.

The immune response plays a vital role in identifying and neutralizing foreign substances, making immunomodulatory assessment crucial for evaluating new compounds.[42] In this study, THP-1 monocytic cells, a well-established model for studying monocyte/macrophage function, were used to examine the effects of TGC and its metabolites.[43] Initial cytotoxicity screening *via* MTS assay confirmed that none of the tested samples were toxic to THP-1 cells as evidenced in Fig. 6e.

Subsequent analysis focused on cytokine release, measuring proinflammatory (IL-6, TNF-α) and anti-inflammatory (IL-10) cytokines in both unstimulated and LPS-stimulated (0.5 μg mL^{-1}) models. Results showed no significant changes in IL-6 or IL-10 secretion following treatment with TG or its metabolites (see Fig. 6f and g). However, TNF-α production increased 1.5- to 2.1-fold in LPS-stimulated cells treated with NF and AuNPs@TiO_2@NF metabolites, whereas AuNPs@TiO_2 metabolites led to a significant decrease. This suggests that AuNPs@TiO_2-catalyzed degradation may render TG into non-immunogenic byproducts.

An essential aspect of drug safety assessment is determining metabolic stability and potential drug–drug interactions, often mediated by cytochrome P450 enzymes (CYP450). To evaluate this, HepG2 cells, a standard model for hepatic metabolism studies,[44] were treated with TG and its metabolites. At 10 μL, no cytotoxicity was observed, but increasing the dose to 100 μL resulted in a significant decline in viability for TG-treated cells, indicating a dose-dependent effect. Metabolic activity assays revealed that AuNPs@TiO_2@NF metabolites enhanced cellular

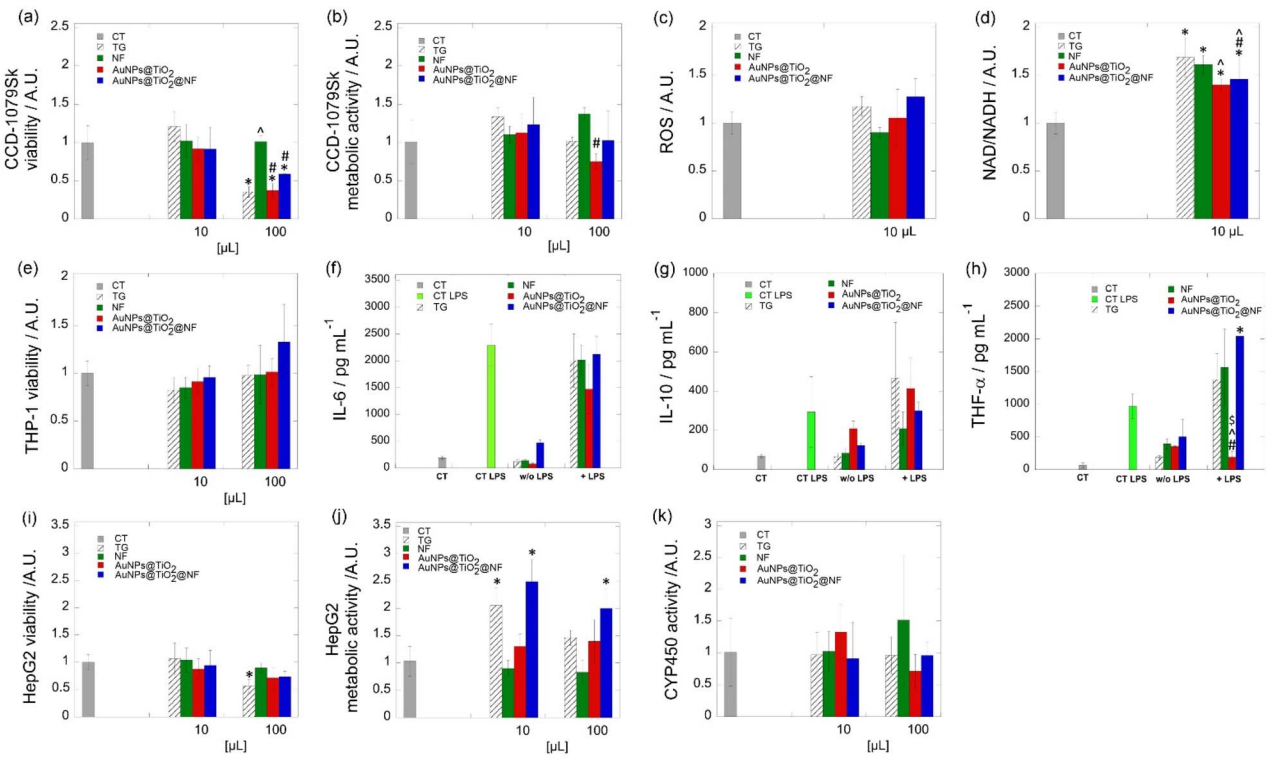

Fig. 6 Biocompatibility of TG and its metabolites in human fibroblasts: (a) cell viability, (b) metabolic activity, (c) ROS levels, (d) NAD^+/NADH ratio (after 24 h exposure). (e) Effects of TG and its metabolites on viability of THP-1 monocytes after 24 h exposure. (f–h) Cytokine release profiles: (f) IL-6, (g) IL-10, and (h) TNF-α levels in both unstimulated and LPS-stimulated conditions. Effects of TG and its metabolites on HepG2 cells after 24 h exposure: (i) viability, (j) metabolic activity, and (k) CYP3A4 enzyme activity. Statistical significance ($p \leq 0.05$): * *vs.* control; ^ *vs.* TG; # *vs.* NF; $ *vs.* AuNPs@TiO_2@NF. Results represent mean ± SD of triplicate measurements, normalized to control.

metabolism at both concentrations. However, CYP3A4 activity remained unaffected regardless of treatment dose, suggesting that TG and its metabolites do not interfere with this key metabolic pathway.

In summary, this study demonstrates that while high concentrations (100 μL) of TG and certain metabolites can reduce cell viability, their impact on metabolic activity, redox balance, and CYP3A4 function is minimal. Notably, AuNPs@TiO_2-catalyzed degradation may mitigate immunogenic effects, highlighting its potential in reducing antibiotic-induced immune responses. These findings contribute to a better understanding of TG's safety profile and its photocatalytic degradation products.

Conclusions

This study presents a breakthrough multifunctional catalyst–gold-embedded TiO_2@NF—that merges photocatalytic degradation with electrocatalytic sensing capabilities. The innovative design leverages SiO_2-templated porosity to maximize surface area, while strategically positioned AuNPs and nickel cobaltite work in concert to enhance visible-light activity and enable magnetic recovery. Beyond its remarkable degradation efficiency, the composite demonstrates practical versatility through sensitive electrochemical H_2O_2 detection, confirming its dual environmental applications.

Rigorous biological testing validates the system's safety profile: degradation products showed minimal cytotoxicity across three human cell lines (fibroblasts CCD-1079Sk, THP-1 monocytes, and HepG2 hepatocytes), with less than 15% viability reduction in MTT assays. Importantly, the treatment preserved 82% of CYP3A4 activity that would otherwise be inhibited by untreated antibiotic residues, addressing a critical concern in pharmaceutical pollution. The composite's negligible immunomodulatory effects, even under inflammatory (LPS-stimulated) conditions, further support its environmental compatibility.

By successfully integrating (1) efficient solar-driven photocatalysis, (2) precise electrocatalytic sensing, and (3) thorough toxicity validation, this work establishes a new standard for designing environmentally safe, multifunctional remediation materials. The demonstrated synergy between catalytic performance and biological safety marks significant progress toward practical water treatment solutions.

Methods

Synthetic procedures

Synthesis of AuNPs. The 20 mL of the $HAuCl_4 \cdot H_2O$ solution (8 mg) was heated until it reached 105 °C. Then, the sodium citrate solution was added. Heating was maintained until the solution turned red, and for 10 minutes more. After cooling to room temperature, the obtained solution was filtered through the syringe filter (0.2 μm). The obtained filtrate was stored in a dark glass bottle in the fridge.

Synthesis of AuNPs@SiO_2. To the thus obtained solution of AuNPs, 4.2 mL of ethanol were added, and subsequently, TEOS (0.36 mL) was added dropwise. The reaction mixture was left stirring for 20 hours at room temperature. Thus the obtained mixture was centrifuged (5 min, 3074×*g*). The supernatant was discarded, while the precipitate was washed with water and ethanol three times. After drying at 80 °C overnight, the obtained solid was ground in a mortar and denoted as AuNPs@SiO_2.

Synthesis of AuNPs@SiO_2@TiO_2. The AuNPs@SiO_2 (20 mg) was suspended in ethanol through brief sonication. The glacial acetic acid was added to reach pH 4. Further, TBOT (1.6 mmol, 0.55 mL) was introduced dropwise. At this moment, the temperature was increased to 45 °C, and the reaction mixture was left stirring for 20 hours. The dry solids were ground in a mortar and calcinated at 450 °C for 2 hours with a temperature ramp of 10 °C min^{-1}.

Synthesis of AuNPs@TiO_2. The AuNPs@SiO_2@TiO_2 (40 mg) was suspended in water and heated to 50 °C. Further, 50 μL of 2.5 mol L^{-1} sodium hydroxide was added. The temperature was increased to 70 °C and the reaction mixture was left stirring for 20 hours. The obtained solid material was ground in a mortar. The completeness of the removal of SiO_2 was verified using the SEM-EDX technique.

Synthesis of AuNPs@TiO_2@NF. The AuNPs@TiO_2 composite (38 mg) was placed in a round bottle flask together with nickel nitrate hexahydrate (0.727 g), iron(III) nitrate nonahydrate (2.02 g), and 25 mL of water. The reaction mixture was heated to 60 °C. Further, citric acid (1.576 g) was introduced. After 20 minutes of stirring at 60 °C, concentrated ammonia was added dropwise until pH 7. Then, the temperature was increased to 80 °C and left for 2 hours until reaching a gel texture. Finally, heating at 130 °C for 20 hours afforded the yellow-greenish solid. It was calcinated at 800 °C for 2 hours with the heating ramp of 10 °C min^{-1}, yielding AuNPs@TiO_2@NF.

Physical characterization

The powder X-ray diffraction data were measured at 293 K using a SuperNova diffractometer with a charge-coupled device (CCD) and a Cu-Kα radiation source at a 158 mm sample-to-detector distance. The crystallite size was calculated using the Scherrer equation: $d_{(100)} = k\lambda/(\beta\cos\theta)$, where $d_{(100)}$ is the particle diameter calculated based on the most intense reflex, in this case (100), k is the Scherrer constant of 0.9, λ is the wavelength of the beam source, β is the full width at half maximum of the (100) reflex in radians, and θ is the Bragg angle. TEM images were obtained by a transmission electron microscope Tecnai T20 G2 X-TWIN (FEI) system operating at an electron beam accelerating voltage of 200 keV. Scanning electron microscopy images were recorded by secondary electron SEM with the use of an INSPECT S50 scanning electron microscope from FEI. The accelerating voltage of the electron beam was 25 keV, and the working distance was 10 mm. Nitrogen adsorption/desorption measurements were performed using an ASAP2020 (Micromeritics Corp., USA) gas sorption system cooled with liquid nitrogen. Samples were degassed under an argon atmosphere for 16 hours at 100 °C. Nitrogen adsorption–desorption isotherms were used to calculate Brunauer–Emmett–Teller (BET) specific surface area and Barrett–Joyner–Halenda (BJH) pore size using Micromeritics MicroActive software. Room-temperature (300 K) magnetization curves were

acquired with a Quantum Design MPMS XL SQUID system (applied field range ±5 T). Samples were prepared as powders in diamagnetic gelatin capsules, with capsule signals subtracted from the raw data. The FTIR spectra were collected at room temperature in the range 400–4000 cm^{-1} using a Nicolet iN10 MX spectrometer (Thermo Scientific). Diffuse reflectance UV-Vis-NIR spectra were recorded on a Jasco V-30 UV-Vis/NIR spectrophotometer equipped with an integrating sphere 60 mm in diameter using $BaSO_4$ as a reference. The zeta potential was determined by means of NanoPlus-3 zeta/nanoparticle analyzer (Micromeritics Instrument Corporation) for aqueous solutions.

Electrochemical studies

Electrocatalytic detection of hydrogen peroxide was carried out in 0.01 mol L^{-1} phosphate buffer solution (PBS) (pH = 7.4) using a PGSTAT 302N potentiostat (Autolab B.V., Metrohm, Utrecht, the Netherlands) in a three-electrode system. Argon was purged into the solution to remove dissolved oxygen for 30 minutes before and after each analyte addition. Prior to surface modification, the working glassy carbon electrode (GCE) (φ 1.6 mm, Bioanalytical Systems Inc.) was polished with 0.3 μm alumina slurries. The electrode was then ultrasonically washed in ethanol and distilled water, dried under an argon atmosphere, and finally modified with carbon paste by applying 20 μL of ethanolic solution of conductive carbon paint (CP, SPI Supplies, USA) containing synthesized material (3 mg mL^{-1}) and evaporating the solvent. The counter electrode was made of platinum mesh (0.25 mm), while a silver wire immersed in 0.1 mol L^{-1} AgCl and separated from the working electrode by a ceramic tip (Bioanalytical Systems Inc.) served as the reference electrode. The AUTOLAB system was controlled with Nova 2.1 software from the same manufacturer. Electrochemical impedance spectroscopy (EIS) studies were carried out in 0.01 mol L^{-1} phosphate buffer solution (PBS) (pH = 7.4) using a PGSTAT 302N potentiostat (Autolab B.V., Metrohm, Utrecht, The Netherlands) in the frequency range of 0.1–100 kHz. Mott–Schottky analysis was performed using an amplitude of 10 mV at 1 Hz for a potential varying from +1 V to −2 V.

Photocatalytic studies

The photocatalytic degradation experiments were investigated in a 50 mL glass cell. The solar light was generated by the SUNTEST CPS+ (ATLAS) simulator equipped with a 1000 Xe lamp. The 20 mL of the tigecycline (TC) solution (4×10^{-5} mol L^{-1}) were irradiated for 2 hours with 15-minute breaks. Catalyst concentration was kept at 1.5 g L^{-1}. Catalyst was separated either by centrifugation (in case of AuNPs@TiO_2, at 3000×*g* for 5 min) or using a neodymium magnet (in case of AuNPs@TiO_2@NF and NF@TiO_2@AuNPs). In order to perform mechanistic studies, we used as scavengers 1,4-benzoquinone (BQ), dimethyl sulfoxide (DMSO), ammonium oxalate (AO), and isopropyl alcohol (i-PrOH), each at a constant concentration of 0.5 mg mL^{-1}. All solutions were prepared with MilliQ water.

Identification of the TG photodegradation products was performed using a Shimadzu Nexera ultra high-performance liquid chromatograph with a photodiode array detector and a triple quadrupole mass spectrometer (Shimadzu LCMS-8040) equipped with an electrospray ionization (ESI) interface. The ESI source operated in negative ionization mode with the capillary voltage at 4.5 kV and the sampling cone at 40 V. The source temperature and desolvation temperature were set to 400 °C and 225 °C, respectively. The mass spectrometry analysis was performed in a full scan (data acquired from 50 to 1000 *m*/*z*), selected ion monitoring (SIM) and multiple ion monitoring (MRM) modes. The MRM analysis included 7 events corresponding to 5 precursor ions with *m*/*z* of 461.45, 460.16, 447.14, 443.15, 433.1 and their respective product ions. Chromatographic separation was performed on a Kinetex C18 column (2.1 mm × 150 mm, 2.6 μm particle diameter), which was maintained at 25 °C. The gradient elution was performed at a flow rate of 0.2 mL min^{-1}. The mobile phase consisted of ammonium formate (5×10^{-3} mol L^{-1}) in 0.01% aqueous formic acid solution (A) and ammonium formate (5×10^{-3} mol L^{-1}) in 0.01% methanol formic acid solution (B). The initial ratio of A : B was 99 : 1 (v/v). The gradient was changed from 1% B (0 min) to 50% B (10 min) and maintained at that level for an additional 10 minutes.

Biological studies

Details about the used cell lines, cell viability assay, and the mode of action studies are included in SI.

Author contributions

Joanna Breczko: investigation, writing original draft, Anna Basa: investigation, Katarzyna Niemirowicz-Laskowska: investigation, writing original draft, Beata Skonieczna: investigation, Raúl López Martín: investigation, writing original draft, José Ángel de Toro Sánchez: writing original draft, Halina Car: formal analysis, editing, funding acquisition, Elzbieta Regulska: conceptualization, supervision, project administration, funding acquisition, investigation, writing – original draft, formal analysis, data curation, review and editing.

Conflicts of interest

There are no conflicts to declare.

Data availability

Data will be made available on request.

Supplementary information is available. See DOI: https://doi.org/10.1039/d5ra06637a.

Acknowledgements

The authors are grateful to Dr Przemysław Wielgat and Dr Anna Sadowska to help in culture preparation. E. R. acknowledges support from the Spanish Ministry of Universities and the European Union's Next Generation Funds through the Maria Zambrano-UCLM grant and Ramon y Cajal funding. This study forms part of the Advanced Materials programme and was supported by MCIN with funding from the European Union NextGenerationEU (PRTR-C17.I1) and the Junta de Comunidades de Castilla-La Mancha. RLM and JAdT acknowledge financial

support from the Agencia Estatal de Investigación (PID2022-142267-I00) and the Junta de Castilla-La Mancha (SBPLY/21/180501/000226). Instrumentation funding was provided by EU Operational Programme Development of Eastern Poland (POPW.01.03.00-20-034/09-00, POPW.01.03.00-20-004/11-00).

Notes and references

1 A. Du Plessis, *One Earth*, 2022, **5**, 129–131.
2 L. Lin, H. Yang and X. Xu, *Front. Environ. Sci.*, 2022, **10**, 880246.
3 R. Hofman-Caris and J. Hofman, in *Applications of Advanced Oxidation Processes (AOPs) in Drinking Water Treatment*, ed. A. Gil, L. A. Galeano and M. Á. Vicente, Springer International Publishing, Cham, 2017, vol. 67, pp. 21–51.
4 M. Ahmed, M. O. Mavukkandy, A. Giwa, M. Elektorowicz, E. Katsou, O. Khelifi, V. Naddeo and S. W. Hasan, *npj Clean Water*, 2022, **5**, 12.
5 E. Regulska, P. Olejnik, H. Zubyk, J. Czyrko-Horczak, M. N. Chaur, M. Tomczykowa, O. Butsyk, K. Brzezinski, L. Echegoyen and M. E. Plonska-Brzezinska, *RSC Adv.*, 2020, **10**, 10910–10920.
6 E. Regulska, J. Breczko and A. Basa, *Diamond Relat. Mater.*, 2022, **128**, 109310.
7 J. Shamshad and R. Ur Rehman, *Environ. Sci.:Adv.*, 2025, **4**, 189–222.
8 S. K. Srivastava, *RSC Appl. Interfaces*, 2024, **1**, 340–429.
9 S. B. Beil, S. Bonnet, C. Casadevall, R. J. Detz, F. Eisenreich, S. D. Glover, C. Kerzig, L. Næsborg, S. Pullen, G. Storch, N. Wei and C. Zeymer, *JACS Au*, 2024, **4**, 2746–2766.
10 X. Li, Y. Chen, Y. Tao, L. Shen, Z. Xu, Z. Bian and H. Li, *Chem Catal.*, 2022, **2**, 1315–1345.
11 N. Anwesha, D. Tripathy, B. B. Sahu, K. Deshmukh and S. Moharana, in *Gold Nanoparticles, Nanomaterials and Nanocomposites*, Elsevier, 2025, pp. 449–491.
12 N. Ghorai, Z. Yang, S. T. Gebre, S. Wu, F. Zhao, I. N. Ivanov and T. Lian, *Nano Lett.*, 2025, **25**, 3253–3258.
13 H. Martínez, J. A. Vergara-Torres, Á. A. Amaya, O. F. Martínez, C. C. Torres and C. H. Campos, *ChemCatChem*, 2025, e202500034.
14 K. Li and J. Wang, *Powder Technol.*, 2025, **460**, 121078.
15 X. Jin, J.-Y. Wu, J. Wang, C.-Y. Chen, T. Kurioka, M. Sone, Y.-J. Hsu, S. Okamoto and T.-F. M. Chang, *ACS Appl. Nano Mater.*, 2025, **8**, 9066–9076.
16 K. Niemirowicz-Laskowska, A. Basa, J. Breczko, I. Kiszkiel-Taudul, P. Wielgat, B. Skonieczna, H. Car and E. Regulska, *Surf. Interfaces*, 2025, **58**, 105889.
17 D. A. Panayotov, A. I. Frenkel and J. R. Morris, *ACS Energy Lett.*, 2017, **2**, 1223–1231.
18 L. El Gaini, *Desalin. Water Treat.*, 2024, **320**, 100798.
19 K. F. Vejchakul and M. Ogawa, *ACS Appl. Nano Mater.*, 2025, **8**, 3402–3412.
20 G. Geng, P. Chen, B. Guan, Y. Liu, C. Yang, N. Wang and M. Liu, *RSC Adv.*, 2017, **7**, 51838–51846.
21 M. W. Mushtaq, M. Shahbaz, R. Naeem, S. Bashir, S. Sharif, K. Ali and N. A. Dogar, *RSC Adv.*, 2024, **14**, 20230–20239.
22 K. A. Cychosz and M. Thommes, *Engineering*, 2018, **4**, 559–566.
23 Z. K. Karakaş, R. Boncukçuoğlu and İ. H. Karakaş, *J. Phys.: Conf. Ser.*, 2016, **707**, 012046.
24 S. A. Jadhav, S. B. Somvanshi, M. V. Khedkar, S. R. Patade and K. M. Jadhav, *J. Mater. Sci.: Mater. Electron.*, 2020, **31**, 11352–11365.
25 B. Tahir, M. Tahir and N. A. S. Amin, *Clean Technol. Environ. Policy*, 2016, **18**, 2147–2160.
26 D. Chen, S. Ma, X. Zhang, X. Wang, M. Gao, J. Li and H. Wang, *RSC Adv.*, 2021, **11**, 1668–1678.
27 U. Ciesla and F. Schüth, *Microporous Mesoporous Mater.*, 1999, **27**, 131–149.
28 P. S. Ramaripa, K. D. Modibane, W. M. Seleka, T. R. Somo, E. Makhado, K. Makgopa and T. B. Ogunbayo, *Int. J. Electrochem. Sci.*, 2024, **19**, 100444.
29 S. He, L. Zhang, S. He, L. Mo, X. Zheng, H. Wang and Y. Luo, *J. Nanomater.*, 2015, **2015**, 659402.
30 A. A. Said, A. A. Abu-Sehly, A. Z. Mahmoud, H. Ahmed and M. N. Goda, *J. Mater. Sci.: Mater. Electron.*, 2022, **33**, 16805–16817.
31 R. B. P. Rivera, R. B. Unabia, R. L. D. Reazo, M. A. Lapening, R. M. Lumod, A. G. Ruda, J. L. Omping, M. R. D. Magdadaro, N. L. B. Sayson, F. S. Latayada, R. Y. Capangpangan, G. G. Dumancas, R. M. Malaluan, A. A. Lubguban, G. C. Petalcorin and A. C. Alguno, *ACS Omega*, 2024, **9**, 33652–33661.
32 C. Dorn, A. Kratzer, U. Liebchen, M. Schleibinger, A. Murschhauser, J. Schlossmann, F. Kees, P. Simon and M. G. Kees, *J. Pharm. Sci.*, 2018, **107**, 739–744.
33 S. Chkoundali, S. Ammar, N. Jouini, F. Fiévet, P. Molinié, M. Danot, F. Villain and J.-M. Grenèche, *J. Phys.: Condens. Matter*, 2004, **16**, 4357.
34 E. Banks, N. H. Riederman, H. W. Schleuning and L. M. Silber, *J. Appl. Phys.*, 1961, **32**, S44–S45.
35 F. Salman, A. Zengin and H. Çelik Kazici, *Ionics*, 2020, **26**, 5221–5232.
36 Mounesh and K. R. Venugopala Reddy, *Anal. Chim. Acta*, 2020, **1108**, 98–107.
37 A. Hankin, F. E. Bedoya-Lora, J. C. Alexander, A. Regoutz and G. H. Kelsall, *J. Mater. Chem. A*, 2019, **7**, 26162–26176.
38 G. Rekhila, Y. Gabes, R. Brahimi, Y. Bessekhouad, O. Mahroua and M. Trari, *J. Sol-Gel Sci. Technol.*, 2018, **85**, 677–683.
39 E. Regulska, J. Breczko, A. Basa, K. Niemirowicz-Laskowska and I. Kiszkiel-Taudul, *Mater. Sci. Eng., B*, 2022, **285**, 115959.
40 B. Poljsak, V. Kovač and I. Milisav, *Oxid. Med. Cell. Longev.*, 2020, **2020**, 1–12.
41 J. S. Teodoro, A. P. Rolo and C. M. Palmeira, *Toxicol. Mech. Methods*, 2013, **23**, 297–302.
42 O. Vargas-Hernández, J. L. Ventura-Gallegos, M. L. Ventura-Ayala, M. Torres, A. Zentella and S. Pedraza-Sánchez, *Cell. Immunol.*, 2020, **355**, 104146.
43 H. Bosshart and M. Heinzelmann, *Ann. Transl. Med.*, 2016, **4**, 438.
44 J. M. Choi, S. J. Oh, S. Y. Lee, J. H. Im, J. M. Oh, C. S. Ryu, H. C. Kwak, J.-Y. Lee, K. W. Kang and S. K. Kim, *Arch. Pharm. Res.*, 2015, **38**, 691–704.